

Design, Kinematics, and Deployment of a Continuum Underwater Vehicle-Manipulator System

Justin Sitler

Department of Mechanical Engineering
Stevens Institute of Technology
Hoboken, NJ 07030
Email: jsitler1@stevens.edu
Student Member, ASME

Long Wang *

Department of Mechanical Engineering
Stevens Institute of Technology
Hoboken, NJ 07030
Email: lwang4@stevens.edu
Member, ASME

Underwater vehicle-manipulator systems (UVMSs) are underwater robots equipped with one or more manipulators to perform intervention missions. This paper provides the mechanical, electrical, and software designs of a novel UVMS equipped with a continuum manipulator, referred to as a continuum-UVMS. A kinematic model for the continuum-UVMS is derived in order to build an algorithm to resolve the robot's redundancy and generate joint space commands. Different methods to optimize the trajectory for specific tasks are proposed using both the weighted least norm solution and the gradient projection method. Kinematic simulation results are analyzed to assess the performance of the proposed algorithm. Finally, the continuum-UVMS is deployed in an experimental demonstration in which autonomous control is tested for a given reference trajectory.

1 Introduction

Underwater robotics is a growing field of research with practical applications including exploration [1], inspection [2], and aquaculture [3]. Recently there is a push in this field towards the development of intervention capabilities via an integrated manipulator, creating an underwater vehicle-manipulator system (UVMS). Design and control of a free-floating UVMS is a very challenging problem due to the physical design requirements imposed by the harsh environment, presence of significant and unpredictable disturbances, difficulty in modeling, and environmental barriers to communication.

An important motivation for this research is the development of low-cost solutions for underwater robotics. Many examples of autonomous underwater vehicles (AUVs) and UVMS are large and expensive, such as the Girona 500 I-AUV [4, 5], or SAUVIM [6, 7]. To lower the barrier of entry, there has been recent work towards the development of small-scale platforms such as the Blue Robotics BlueROV2 [8] remotely operated vehicle (ROV), which has been used in work by Marais et. al. [9] as well as McConnell et. al. [10]. To this end, this paper provides the design and integration of a UVMS with a small and low-cost vehicle and manipulator.

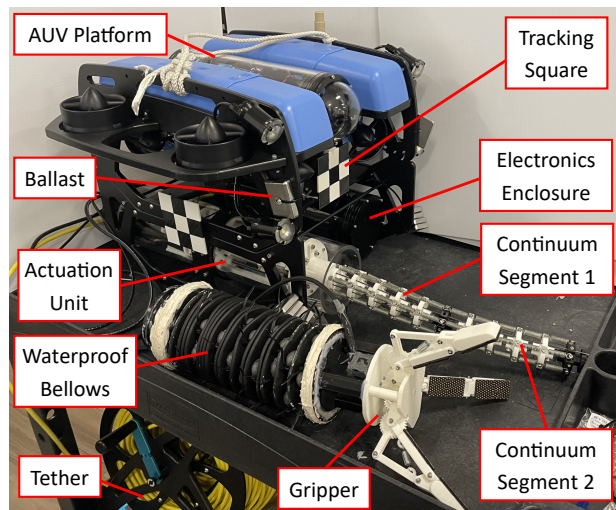


Fig. 1: Continuum-UVMS integration schematic.

*Corresponding author.

The manipulator design proposed in this paper is a continuum manipulator, an unconventional class of robots characterized by high flexibility and compliance allowing them to achieve continuous articulating profiles. There has been limited research on continuum manipulators in field robotics or underwater applications specifically; for more detail, see Section 2. However, many features of this class of manipulators make them beneficial for underwater manipulation. The first is their natural passive compliance, which is useful in intervention tasks because it compensates for positioning error and mitigates contact forces. In addition, continuum manipulators are comparatively lightweight and most of their mass is centralized in an actuation unit. This means that inertial coupling between the manipulator and the vehicle is reduced, allowing the manipulator to be neglected and thus simplifying vehicle control. Finally, the flexibility of a continuum manipulator makes them particularly useful in constrained environments, which in sub-sea applications may include a natural crevice or a man-made structure such as a pipe or propeller.

By combining a continuum manipulator with a free-floating vehicle platform, we introduce the novel continuum-UVMS in this paper. This design is distinguished from typical UVMSs which use serial manipulators, such as the aforementioned Girona 500 I-AUV or SAUVIM. Research on underwater continuum manipulators typically are not integrated to a free-floating vehicle [11–13] and thus are not classified as UVMSs. Ma et. al. [14] has proposed a similar continuum-UVMS design but has not integrated the continuum manipulator with the vehicle. Gong et. al. [15] used a soft manipulator with an ROV platform that could be considered a continuum robot, but did not consider coordinated motions of the vehicle and manipulator. In addition, this soft manipulator is distinguished from this design through the use of a rigid backbone and tendon actuation similar to “elephant trunk” continuum manipulator designs [16, 17], which have not yet been used underwater.

This paper introduces two primary unique contributions to UVMS design and control:

- Design and integration of an open-source waterproof continuum manipulator onto a free-floating underwater vehicle platform, forming a novel continuum-UVMS. In addition, the continuum-UVMS is deployed in a controlled environment to demonstrate both teleoperational and autonomous control of the UVMS.
- Kinematics of the continuum-UVMS and development of the optimized redundancy resolution algorithm for position control of the UVMS via null-space gradient projection. The autonomous execution of the end-effector trajectory is performed both in kinematic simulation and experimentally through coordinated control of the manipulator and vehicle to highlight the impact of optimization as well as the functionality of the hardware.

This paper is outlined as follows. Section 2 provides a brief literature review of the development of UVMSs, the different control and optimization methods used for these sys-

tems, and examples of continuum manipulators for various field applications. Section 3 discusses the mechanical design of the continuum manipulator and how it is integrated with the vehicle platform. Section 4 describes the derivation of the differential kinematics for the robotic system, implementation of the redundancy resolution algorithm, and optimization of the algorithm with respect to secondary tasks. In Section 5, we validate the algorithm in simulation to validate the optimization. Finally, in Section 6, the continuum manipulator and vehicle are combined in an underwater experiment to demonstrate the capabilities of the continuum-UVMS.

2 Related Works

2.1 Redundancy Resolution Problem of UVMS

Mission tasks for a UVMS can be broken into two main categories of realistic intervention tasks [18]. The first task involves autonomously docking the UVMS and then performing a desired intervention task with the manipulator [19] while the second more challenging task involves free floating intervention [20]. These tasks have been solved by using a kinematic control layer to generate vehicle and manipulator trajectories and a dynamic control layer to achieve the desired commands. A dynamic controller was optimized for drag minimization in [21], and a recent work used sliding mode control for UVMS in [22].

The kinematic control problem for a UVMS has kinematic redundancy, since the combined DoFs of the vehicle and manipulator exceed the minimally required DoFs of a given manipulator task in Cartesian space. This means the robot can perform additional subtasks while still satisfying its primary task. One method to do so is the gradient projection method, developed in [23] and also implemented in more recent works such as [24, 25] which both used the method to avoid obstacles. Task priority control is another method to resolve this problem [26] and has been implemented in more recent works such as [27]. A third method to solve the problem is through a weighted least norm solution [28]. Other methods for subtask resolution and redundant control have been implemented as well, including combination of the weight least norm solution and gradient projection methods [29] or null space saturation to avoid joint constraints and ensure feasibility of the command [30, 31].

Application of these kinematic control methods for UVMSs has been the focus of works since the early 2000’s. The gradient projection method was implemented in [21, 32] to minimize drag forces. The task priority method was implemented in [29, 33, 34] to maintain joint limits, manipulability, horizontal attitude, and camera field of view. A detailed summary of the modelling and control of AUVs and UVMSs can be found in [35]. It is worth noting that these works are all validated in simulation; other works such as [20, 36] validated a task priority method experimentally using the Girona 500 TRIDENT configuration.

2.2 Manipulator Design and Continuum Manipulators

The manipulator design is crucially important to the functionality of the UVMS. Commercially available underwater arms for use on smaller ROVs or AUVs are listed in [37]; however, these designs are large and heavy rigid-link manipulators, with weights ranging from 10 kg to over 50 kg. Many of these are powered via hydraulic systems, although electric-powered arms are also available. The Graal Tech underwater modular arm (UMA) is actuated by brushless motors and has been used frequently with the Girona 500 I-AUV [20]. The cost and bulk of these manipulators have led some to design and build smaller, more affordable solutions; [38] designed and experimentally validated a lightweight four DoF arm and gripper actuated by servomotors contained in a centralized waterproof unit. In addition, Reach Robotics [39] has developed small, dexterous serial manipulators intended for use on small ROV platforms; for example, in [9] the BlueROV2 platform [8] was used as a small and inexpensive vehicle in conjunction with the Reach Alpha.

An unconventional manipulator design is the continuum robot, a flexible manipulator so named because of its ability to achieve continuous circular bending motion, compared to traditional manipulators which consist of a series of discrete rigid links. A classic example of a continuum manipulator is in [16] and [17], which detail the design and kinematic control of the ‘elephant’s trunk’ manipulator, a four-segment, eight-DoF, tendon-driven continuum manipulator that mimics the motion and grasping capabilities of an elephant’s trunk. Their compliant and hyper-redundant design makes them difficult to estimate shape and control position, which has been the focus of recent works such as [40–43]. There are some examples of field applications of continuum manipulators as well, such as the pneumatically-actuated OctArm manipulator [44].

The utility of continuum manipulators for underwater applications is discussed in [45], which claims their passive compliance and small number of moving parts as attractive features in an underwater environment. Potential use cases cited include grasping, visual or acoustic inspection, and bio-mimetic vehicle propulsion. A bio-inspired octopus robot with eight continuum manipulators for grasping and locomotion was proposed in [12, 46]. A continuum manipulator was attached onto the SILVER2 underwater crawler for grasping small objects on the seafloor in [13]. The AMADEUS dexterous sub-sea hand [11] uses three small hydraulically-actuated continuum fingers for an underwater gripper. In our previous work, we developed a compact, low cost, and easy to fabricate underwater continuum manipulator [47], but integration with the vehicle was not addressed.

Two recent works are most relevant to our proposed approach. A hydraulic soft manipulator was proposed in [15] which was attached to a free-floating underwater vehicle for delicate grasping in shallow water. It is worth noting that the vehicle was intended to be stationary on the seafloor during tasks. A prototype six DoF continuum manipulator for use on a UVMS was also introduced and tested in [14]. The total system, which uses two arms with unique end-of-arm tooling

connected to an ROV platform, is very similar to the concept and design proposed in this paper. However, it is worth noting that [14] only provides in-air testing of the continuum manipulator.

3 Continuum-UVMS Design

3.1 Continuum Manipulator Design

The continuum robot arm used in this paper is a two-segment multi-backbone design adapted from the design developed in our previous work [47]. The most significant change in the continuum manipulator design is the addition of a second continuum segment, giving the entire arm a total of four DoFs. This allows the distal portion of the arm to bend independently from the proximal portion, increasing its maneuverability and dexterity. The continuum manipulator is actuated via two sets of three nitinol wires which pull on the end link of each segment. The wires are connected to an actuation unit which creates the linear pulling motion via six lead screws and servo motors inside a waterproof enclosure. A gearbox was designed to change the axis of rotation and allow the servomotors to be mounted more compactly. A flexible bellows with distributed ballast covers the continuum manipulator to make the whole system waterproof and neutrally buoyant. A schematic of the manipulator can be seen in Fig. 2, in which the enclosure tube and bellows are hidden for clarity. The CAD models, components list, and assembly instructions for this design are open-source and available in [48].

In addition, a 3D printed three-finger waterproof gripper is attached to the end of the continuum manipulator. This gripper, shown in Fig. 3, uses an under-actuated design similar to the one proposed in [49], with a single motor actuating three 2-DoF fingers simultaneously via a 3D printed worm gear. This gear meshes with two spur gears to actuate the first DoF of the finger through a four-bar mechanism. The second DoF of each finger is actuated passively through the use of a stainless steel extension spring. The use of a worm gear allows for relatively high torque output and a simpler assembly when compared with a tendon driven under-actuated gripper. The servo motor casing is completely sealed via epoxy, and an O-ring ensures water will not leak through the motor shaft. The 3D printed and stainless steel components can be exposed to water, which means the entire gripper can be submerged without the need for a special housing. The motor connects to the rest of the motors and motor controller via a long waterproof cable, potted at the point of entry to ensure the arm enclosure stays sealed. While the actuation of the gripper is not considered in the kinematic control algorithm proposed in this paper, it is integrated in the experiments for verisimilitude of a real grasping task.

3.2 Integration with Vehicle

The underwater vehicle used in this paper is the BlueROV2 by Blue Robotics, Inc. [8]. This platform was chosen because of its low cost and ease of integration via an additional payload skid, customizable waterproof enclo-

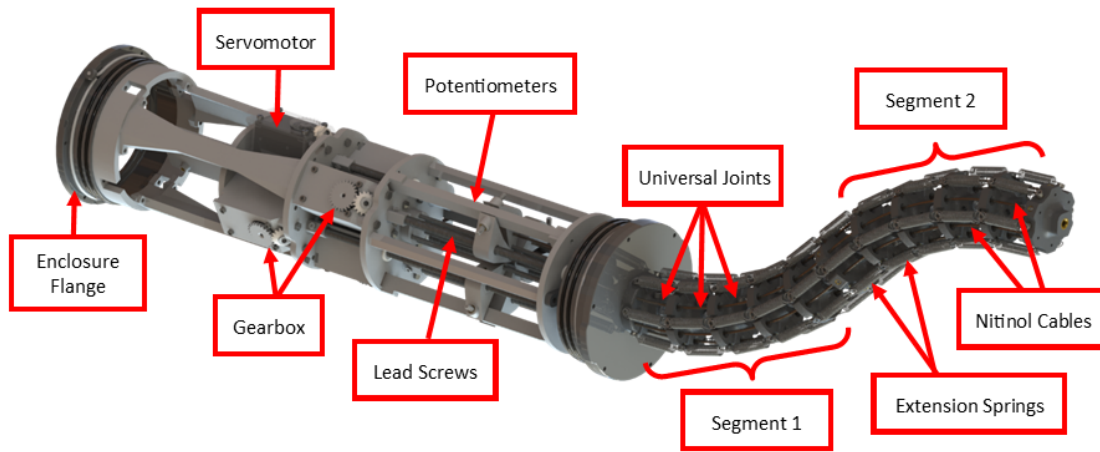


Fig. 2: Two segment continuum manipulator schematic.

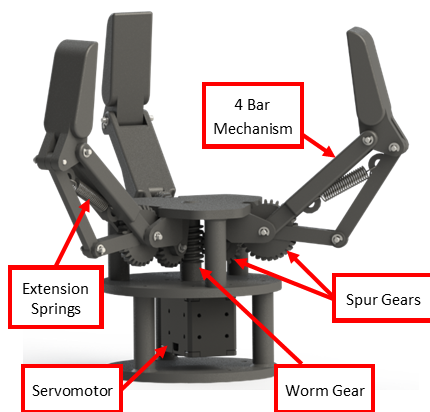


Fig. 3: Underactuated gripper schematic.

sures and penetrators, and the Heavy Configuration upgrade, which has eight thrusters to allow for six DoF control and improve stability and maneuverability. The continuum manipulator and the electronics enclosure are mounted side-by-side on the payload skid underneath the body of the vehicle. Figure 1 labels the components of the system on the robot, with the waterproof bellows removed for visibility.

The deployed system is broken up into four waterproof enclosures. The actuation unit contains the microprocessors, sensors, and motors required to actuate the continuum manipulator. The electronics enclosure contains a Jetson Nano computer for controlling the continuum manipulator and acts as the central hub for connecting all of the communications and power cables, as well as hosting the VectorNav VN-100 inertial measurement unit (IMU) that measures the vehicle's orientation. Finally, the BlueROV enclosure contains the flight controller, thruster controllers, and power distribution for the vehicle, with additional connections to the vehicle battery stored in a separate enclosure. The BlueROV and battery enclosures are attached to the frame of the vehicle, while the actuation unit and electronics enclosure are mounted on the payload skid on the bottom of the vehicle

via watertight enclosure clamps. Communication between the different enclosures is achieved via underwater cables, and communications between the entire continuum-UVMS and the topside computer is achieved via a single shielded twisted pair waterproof tether. The waterproofing enclosures and underwater cables are from Blue Robotics, Inc. [8]

The topside setup includes a Linux master computer and a tether interface. The Robot Operating System (ROS) Melodic Morenia distribution [50] is used as the software framework for establishing communications between the various components in the system. The desired end-effector pose is provided by the user and is presumed to be a stationary target pose in this paper. The kinematic control algorithm detailed in Section 4 calculates the optimal trajectory to achieve this pose and publishes the desired vehicle state velocities, Ψ_V , and the desired continuum manipulator state, Ψ_M . The vehicle control node subscribes to the desired vehicle state velocities and converts to vehicle velocity commands in the body-fixed frame $\{A\}$, represented by ${}^A\Psi_V$. The continuum control node is adapted from our previous work [47] and publishes motor velocity commands, $\dot{\mathbf{q}}$, based on the current motor position, \mathbf{q} . Communication with the vehicle is done via ROS using the MAVLink messaging protocol on a ROS node that establishes a communications bridge. This bridge receives vehicle velocity commands and sends them to the vehicle autopilot to be executed. The code for establishing the vehicle communications and connecting to the IMU was adapted from [51] and used in works such as [10].

4 Kinematics for the Continuum-UVMS

For many tasks for a UVMS, the robot's end-effector must achieve a specific pose (position and orientation), which requires the system to have six DoFs. However, a UVMS will typically have kinematic redundancy. This means that with careful planning and decision-making, the robot can complete additional subtasks or objectives while still satisfying the primary task constraint. This section will discuss a redundant kinematic control algorithm to resolve

a free-floating manipulator positioning task using a combination of the gradient projection method and weighted least norm solution. This algorithm generates a locally optimal trajectory and publishes the vehicle and manipulator commands in real time via ROS. The relevant works from which this method is adapted are discussed in Section 2.

4.1 Jacobian Derivation

The total Jacobian matrix relates the linear and angular velocities of the end-effector in the global coordinate system (GCS) to the vehicle and continuum manipulator state velocities. To represent the full state of the vehicle and continuum manipulator, the total Jacobian needs to account for the six DoFs from the mobile vehicle pose as well as the four DoFs from the two-segment continuum manipulator. The total state of the robot is represented by the vector Ψ :

$$\Psi = \begin{bmatrix} \Psi_V^T & \Psi_M^T \end{bmatrix}^T, \quad \Psi \in \mathbb{R}^{10 \times 1} \quad (1)$$

$$\Psi_V = \begin{bmatrix} x_A & y_A & z_A & \alpha & \beta & \gamma \end{bmatrix}^T \quad (2)$$

$$\Psi_M = \begin{bmatrix} \theta_1 & \phi_1 & \theta_2 & \phi_2 \end{bmatrix}^T \quad (3)$$

The vector Ψ includes vehicle states Ψ_V and manipulator configuration states Ψ_M . Variables x_A , y_A , and z_A represent the linear position \mathbf{p}_A of the vehicle frame $\{A\}$ relative to the global coordinate system (GCS), represented by frame $\{GCS\}$, with $\mathbf{p}_A = \begin{bmatrix} x_A & y_A & z_A \end{bmatrix}^T$. Variables α , β , and γ represent respectively the yaw, pitch, and roll angles of the vehicle attitude, which can be represented in rotation matrix form by the sequence $\mathbf{R}_A = \mathbf{R}_z(\alpha) \mathbf{R}_y(\beta) \mathbf{R}_x(\gamma)$. Variables θ_i and ϕ_i represent respectively the bending angle and the bending plane direction angle for the i^{th} continuum segment. The pose of the end-effector relative to frame $\{GCS\}$ is defined as:

$$\mathbf{x} = \{\mathbf{p}, \mathbf{R}\} \quad (4)$$

$$\mathbf{p} = \mathbf{p}_A + \mathbf{R}_A {}^A\mathbf{r}_B + \mathbf{R}_B {}^B\mathbf{r}_C + \mathbf{R}_C {}^C\mathbf{r}_D \quad (5)$$

where \mathbf{p} and \mathbf{R} represent the end-effector position and orientation rotation matrix relative to frame $\{GCS\}$, ${}^A\mathbf{r}_B$ represents the position of the base of continuum segment 1 relative to frame $\{A\}$, ${}^B\mathbf{r}_C$ represents the end position of continuum segment 1 relative to frame $\{B\}$, and ${}^C\mathbf{r}_D$ represents the end position of continuum segment 2 relative to frame $\{C\}$. \mathbf{R}_A , \mathbf{R}_B , and \mathbf{R}_C represent respectively the orientation of frame $\{A\}$, $\{B\}$, and $\{C\}$ as shown in Figure 4 in rotation matrix form.

We then will start deriving the total Jacobian matrix:

$$\dot{\mathbf{x}} = \mathbf{J} \dot{\Psi}, \quad \mathbf{J} \in \mathbb{R}^{6 \times 10} \quad (6)$$

where $\dot{\mathbf{x}}$ is the desired end-effector twist. First, we consider

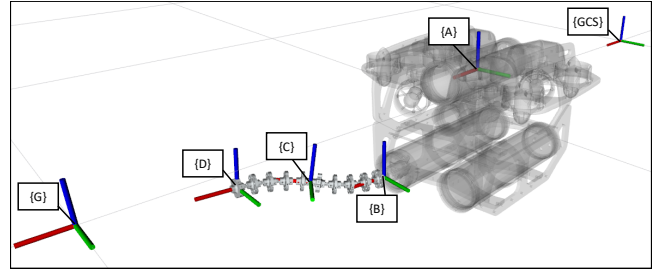


Fig. 4: Continuum-UVMS coordinate frames. $\{GCS\}$ - global coordinate system; $\{A\}$ - vehicle frame; $\{B\}$ - base frame of 1st continuum segment; $\{C\}$ - base frame of 2nd continuum segment; $\{D\}$ - end-effector frame; $\{G\}$ - goal frame.

the configuration-to-task space Jacobian matrix $\mathbf{J}_{c,i}$ for the i^{th} continuum segment:

$$\mathbf{J}_{c,i} = \begin{bmatrix} \mathbf{J}_{p,i} \\ \mathbf{J}_{\mu,i} \end{bmatrix} \quad (7)$$

$$\mathbf{J}_{c,i} \in \mathbb{R}^{6 \times 2}, \mathbf{J}_{p,i} \in \mathbb{R}^{3 \times 2}, \mathbf{J}_{\mu,i} \in \mathbb{R}^{3 \times 2} \quad (8)$$

Derivation of the position and orientation Jacobians, $\mathbf{J}_{p,i}$ and $\mathbf{J}_{\mu,i}$, as well as the continuum segment displacements, ${}^B\mathbf{r}_C$ and ${}^C\mathbf{r}_D$, can be found in [47]. The Jacobians are given by:

$$\mathbf{J}_{p,i} = \frac{l_i}{\theta_i} \begin{bmatrix} \cos \theta_i - \frac{\sin \theta_i}{\theta_i} & 0 \\ \left(\sin \theta_i - \frac{\cos \theta_i - 1}{\theta_i} \right) \cos \phi_i & (\cos \theta_i - 1) \sin \phi_i \\ \left(\sin \theta_i - \frac{\cos \theta_i - 1}{\theta_i} \right) \sin \phi_i & (1 - \cos \theta_i) \cos \phi_i \end{bmatrix} \quad (9)$$

$$\mathbf{J}_{\mu,i} = \begin{bmatrix} 0 & \cos \theta_i - 1 \\ \sin \phi_i & \sin \theta_i \cos \phi_i \\ -\cos \phi_i & \sin \theta_i \sin \phi_i \end{bmatrix} \quad (10)$$

where l_i represents the total length of continuum segment i . The transformation of these Jacobians into the GCS leads to the total Jacobian matrix:

$$\mathbf{J} = \begin{bmatrix} \mathbf{J}_1 & \mathbf{J}_2 & \mathbf{J}_3 \end{bmatrix} \quad (11)$$

$$\mathbf{J}_1 = \underbrace{\begin{bmatrix} \mathbf{I}_{3 \times 3} & \begin{bmatrix} 0 & \mathbf{r}_D^A \end{bmatrix}^T \\ \mathbf{0} & \mathbf{T} \end{bmatrix}}_{\text{Vehicle Velocity}} \quad (12)$$

$$\mathbf{J}_2 = \underbrace{\begin{bmatrix} \mathbf{R}_A & \begin{bmatrix} 0 & \mathbf{r}_D^C \end{bmatrix} \\ \mathbf{0} & \mathbf{R}_A \end{bmatrix}}_{\text{1st Continuum Segment}} \mathbf{J}_{c,1} \quad (13)$$

$$\mathbf{J}_3 = \underbrace{\begin{bmatrix} \mathbf{R}_C & \mathbf{0} \\ \mathbf{0} & \mathbf{R}_C \end{bmatrix}}_{2^{\text{nd}} \text{ Continuum Segment}} \mathbf{J}_{c,2} \quad (14)$$

where $[\mathbf{v}]_{\times}$ represents the skew-symmetric matrix operator on vector \mathbf{v} . Matrix \mathbf{T} represents the relation between Euler-angle rates and body-axis rates and is given by:

$$\mathbf{T} = \begin{bmatrix} 0 & -\sin \alpha & \cos \alpha \cos \beta \\ 0 & \cos \alpha & \sin \alpha \cos \beta \\ 1 & 0 & -\sin \beta \end{bmatrix} \quad (15)$$

This model presumes the vehicle has six degree of freedom control; however, some vehicle platforms only provide four degrees of freedom control (position and yaw). In this case, β and γ can be removed from Ψ , and the corresponding columns (the 5th and 6th) are removed from the total Jacobian matrix \mathbf{J} .

4.2 Redundancy Resolution and Control

We start by considering the weighted minimum norm problem described as below:

$$\begin{aligned} & \text{minimize} && \frac{1}{2} \left(\dot{\Psi}^T \mathbf{W} \dot{\Psi} \right) \\ & \text{subject to:} && \dot{\mathbf{x}} = \mathbf{J} \dot{\Psi} \end{aligned} \quad (16)$$

where $\dot{\mathbf{x}}$ is the desired end-effector twist. The choice of the weighting matrix \mathbf{W} is discussed in more detail in Section 4.3. The weighted least norm solution to this problem is given by:

$$\mathbf{J}_W^+ = \mathbf{W}^{-1} \mathbf{J}^T \left(\mathbf{J} \mathbf{W}^{-1} \mathbf{J}^T \right)^{-1} \quad (17)$$

$$\dot{\Psi} = \mathbf{J}_W^+ \dot{\mathbf{x}} \quad (18)$$

This solution gives the state velocities that satisfy a desired end-effector twist $\dot{\mathbf{x}}$ while minimizing the weighted norm of the state velocity vector $\dot{\Psi}$. The desired end-effector twist must be properly chosen in order to achieve the desired pose. We implement a resolved rates algorithm to resolve in real time the desired linear and angular velocity magnitudes v_{mag} and ω_{mag} until it reaches the goal.

The resolved rates has been implemented alongside the redundancy resolution formulation as described in this section as well as Algorithm 1. The desired linear velocity vector points from the current end-effector position \mathbf{p} to the goal position $\mathbf{p}_G = [x_G \ y_G \ z_G]^T$. As the end-effector approaches the goal, the magnitude will decrease from a constant v_{max} when it is far away to v_{min} as a function of the error threshold e_p as well as scaling parameter λ_p . The desired angular velocity vector is applied along vector \mathbf{m} which is found us-

ing the axis angle representation of the orientation error matrix \mathbf{R}_{err} , which represents the error in orientation between the current end-effector orientation \mathbf{R} and the goal orientation \mathbf{R}_G . Like the desired linear velocity, the desired angular velocity decreases in magnitude from ω_{max} to ω_{min} as a function of the error threshold e_μ and scaling parameter λ_μ .

After the end-effector twist has been calculated, the Jacobian and weighting matrices are updated to reflect the current robot state Ψ . The desired robot state velocities $\dot{\Psi}$ are calculated using the weighted inverse Jacobian and the gradient vector ∇g_j , discussed in more detail in Section 4.4. Then, the commanded robot state is updated for the next time step and published to ROS. The end-effector is considered to have reached the desired pose when the position and orientation errors are within these error thresholds, terminating the algorithm in the case of a fixed goal or continuing in the case of a moving trajectory.

The implementation of this algorithm is referred to in other works as the ‘‘kinematic control layer’’. In this paper, we neglect the dynamics of the vehicle-manipulator system in order to focus on the kinematic modeling and motion control. The algorithm presented is differentiated from other works through the derivation of the UVMS kinematics for a continuum manipulator, and the derivation of objective functions in Section 4.4 for a continuum-UVMS.

4.3 Task Optimization via Weighted Least Norm

A weighted least norm (WLN) solution has been proposed in works such as [28] to solve the redundancy problem. The diagonal weighting matrix \mathbf{W} allows the motion of certain degrees of freedom of the robot to be prioritized or penalized. Higher value weights correspond to higher penalties on the respective degree of freedom. To start, a constant weighting matrix \mathbf{W}_c can be used, with weights found empirically:

$$\mathbf{W}_c = \text{diag} (w_{c1}, w_{c2}, \dots, w_{c10}) \quad (28)$$

$$w_{c1:6} = 1000 \quad (29)$$

$$w_{c7} = w_{c8} = 1 \quad (30)$$

$$w_{c8} = w_{c10} = 0.01 \quad (31)$$

In this paper, two subtasks are proposed for optimization via weighting matrix: joint limit avoidance and dynamic prioritization of the continuum manipulator. The joint limit avoidance task is a classic example of optimization via the WLN method, used in works such as [28] for a traditional robot and [29] for UVMS control. For the continuum manipulator, the only limits are on the bending angles θ_i , which should be less than $\theta_M = \frac{\pi}{3}$ and greater than $\theta_m = -\frac{\pi}{3}$ to prevent stalling the motors or damaging the arm. The bending plane direction angle ϕ_i has no limits, allowing the continuum manipulator to freely rotate in a circular path. Therefore the joint limit weighting matrix, \mathbf{W}_j , should only affect the DoFs corresponding to θ_1 and θ_2 , making these weights tend towards infinity as the manipulator approaches the joint

Algorithm 1 Redundancy Resolution with Resolved Rates

 Initialize: $\mathbf{x}, \leftarrow \mathbf{x}_0, \quad \Psi \leftarrow \Psi_0$

 Goal Pose: $\mathbf{x}_G \leftarrow \{\mathbf{p}_G, \mathbf{R}_G\}$

 Objective Function: $g(\Psi)$
while $\delta_p > e_p \parallel \delta_\mu > e_\mu$ **do**
Step 1 - Get current pose:

 $\mathbf{p}, \mathbf{R} \leftarrow$ Kinematic Model

Step 2 - Compute errors:

$$\delta_p = \sqrt{(\mathbf{p}_G - \mathbf{p})^T (\mathbf{p}_G - \mathbf{p})} \quad (19)$$

$$\mathbf{R}_{\text{err}} = \mathbf{R}_G \mathbf{R}^T, \quad \mu_{\text{err}} = \arccos \frac{\text{Tr}(\mathbf{R}_{\text{err}}) - 1}{2} \quad (20)$$

$$\mathbf{m} = \frac{1}{2 \sin \mu_{\text{err}}} \begin{bmatrix} \mathbf{R}_{\text{err}}^{32} - \mathbf{R}_{\text{err}}^{23} \\ \mathbf{R}_{\text{err}}^{13} - \mathbf{R}_{\text{err}}^{31} \\ \mathbf{R}_{\text{err}}^{21} - \mathbf{R}_{\text{err}}^{12} \end{bmatrix} \quad (21)$$

$$\delta_\mu = \sqrt{(\mu_{\text{err}} \mathbf{m})^T (\mu_{\text{err}} \mathbf{m})} \quad (22)$$

Step 3 - Compute desired end-effector twist:

if $\delta_p/e_p > \lambda_p$ **then**

$$v_{\text{mag}} = v_{\text{max}}$$

else

$$v_{\text{mag}} = v_{\text{min}} + \frac{(v_{\text{max}} - v_{\text{min}}) (\delta_p - e_p)}{e_p (\lambda_p - 1)} \quad (23)$$

end if
if $\delta_\mu/e_\mu > \lambda_\mu$ **then**

$$\omega_{\text{mag}} = \omega_{\text{max}}$$

else

$$\omega_{\text{mag}} = \omega_{\text{min}} + \frac{(\omega_{\text{max}} - \omega_{\text{min}}) (\delta_\mu - e_\mu)}{e_\mu (\lambda_\mu - 1)} \quad (24)$$

end if

$$\text{Desired linear velocities: } \dot{\mathbf{p}} = v_{\text{mag}} \frac{\mathbf{p}_G - \mathbf{p}}{\delta_p}$$

$$\text{Desired angular velocities: } \dot{\boldsymbol{\mu}} = \omega_{\text{mag}} \mathbf{m}$$

$$\text{Desired twist: } \dot{\mathbf{x}} = \begin{bmatrix} \dot{\mathbf{p}} \\ \dot{\boldsymbol{\mu}} \end{bmatrix}^T$$

Step 4 - Compute redundancy resolution:

$$\mathbf{J}, \mathbf{W}, g_j \leftarrow \Psi \quad (25)$$

$$\dot{\Psi} = \mathbf{J}_W^+ \dot{\mathbf{x}} + (\mathbf{I} - \mathbf{J}_W^+ \mathbf{J}) \sum_{j=1}^n k_j \nabla g_j(\Psi) \quad (26)$$

$$\Psi = \Psi + \dot{\Psi} dt \quad (27)$$

end while

limit:

$$\mathbf{W}_j = \text{diag}(w_{j1}, w_{j2}, \dots, w_{j10}) \quad (32)$$

$$w_{j1:6} = w_{j8} = w_{j10} = 1 \quad (33)$$

$$w_7, w_9 = \begin{cases} 1 + \left| \frac{(\theta_M - \theta_m)^2 (2\theta_i - \theta_M - \theta_m)}{4(\theta_M - \theta_i)^2 (\theta_i - \theta_m)^2} \right| & \text{if } \Delta|\theta_i| \geq 0 \\ 1 & \text{if } \Delta|\theta_i| < 0 \end{cases} \quad (34)$$

For the second subtask, the free-floating robot should prioritize using the DoFs corresponding to the vehicle state Ψ_V when the end-effector is far from the target, measured by position error δ_p , because the gross motion required will be

much faster with the vehicle thrusters and possibly outside the workspace of the manipulator alone. However, the robot should prioritize the manipulator state Ψ_M if it is close to the target, as this is more energy-efficient considering the vehicle inertia and manipulator control is generally more precise than vehicle control. A method of addressing this prioritization via WLN has been proposed in [35] through the use of a weight factor η . The weight factor will be slightly modified in this paper to only consider the position error, with manipulator weights becoming large as η approaches 1 and vehicle weights becoming large as η approaches 0. The shape of η as a function of δ_p should be smooth, so a fifth-order smoothing polynomial $S(x, x_m, x_M)$ is used. The manipulator prioritization matrix \mathbf{W}_m is given by:

$$\mathbf{W}_m = \begin{bmatrix} \mathbf{I}_{6 \times 6} \left(\frac{1}{\eta} \right) & \mathbf{0}_{6 \times 4} \\ \mathbf{0}_{4 \times 6} & \mathbf{I}_{4 \times 4} \left(\frac{1}{1-\eta} \right) \end{bmatrix} \quad (35)$$

$$\eta = 0.01 + (0.9 - 0.01) S(\delta_p, 0, \lambda_{\text{pre}}) \quad (36)$$

$$S(x, x_m, x_M) = \begin{cases} 1 & x \geq x_M \\ 6x^5 - 15x^4 + 10x^3 & x_m < x < x_M \\ 0 & x \leq x_m \end{cases} \quad (37)$$

The threshold λ_{pre} will be discussed in more detail in Section 4.4. The total weighting matrix \mathbf{W} is found by combining the three weighting matrices:

$$\mathbf{W} = \mathbf{W}_c \mathbf{W}_j \mathbf{W}_m \quad (38)$$

4.4 Task Optimization via Gradient Projection

Works such as [23] and [25] formulate the gradient projection method (GPM) to maximize an objective function $g(\Psi)$ by projecting its gradient into the null space of the Jacobian:

$$\dot{\Psi} = \underbrace{\mathbf{J}_W^+ \dot{\mathbf{x}}}_{\text{Task Constraint}} + \underbrace{(\mathbf{I} - \mathbf{J}_W^+ \mathbf{J}) k \nabla g(\Psi)}_{\text{Null Space Projection}} \quad (39)$$

where \mathbf{J}^+ denotes the Moore–Penrose (pseudo) inverse of \mathbf{J} . The value of the scaling parameter k changes how strong an affect the gradient has on the state velocities. In addition, a negative value of the scaling parameter minimizes the objective function, while a positive value maximizes it. In this paper, the scaling parameter is a constant found empirically. This is a common practice for determining the scaling parameters, although other works such as [24] and [25] have used a variable scaling parameter to further improve trajectory optimization. If multiple gradient functions are used simultaneously, the weighted sum of each gradient can be used; however, this does not guarantee optimal solutions for each gradient function if the subtasks conflict. This can be avoided by choosing objective functions which are orthogo-

nal to each other. The solution for n subtasks is given by:

$$\dot{\Psi} = \mathbf{J}_W^+ \dot{\mathbf{x}} + (\mathbf{I} - \mathbf{J}_W^+ \mathbf{J}) \sum_{j=1}^n k_j \nabla g_j(\Psi) \quad (40)$$

In this paper, three subtasks will be proposed. The first is to maintain the vehicle in an upright orientation in order to easily control and maneuver it. The objective function associated with this task, g_1 , can be defined as the dot product between the world z axis, $\hat{\mathbf{z}}_{\text{GCS}}$, and the vehicle z axis, $\hat{\mathbf{z}}_A$, which can be shown to be simply the product of the pitch and roll angles:

$$g_1(\Psi) = \hat{\mathbf{z}}_{\text{GCS}}^T \hat{\mathbf{z}}_A = \cos \beta \cos \gamma \quad (41)$$

$$\nabla g_1(\Psi) = \begin{bmatrix} \mathbf{0}_{4 \times 1} \\ -\sin \beta \cos \gamma \\ -\cos \beta \sin \gamma \\ \mathbf{0}_{4 \times 1} \end{bmatrix} \quad (42)$$

The second subtask is to orient the vehicle towards the target. This is important in many applications to allow the camera to clearly see the target. In this paper, this task will only use the orientation in the global XY plane in order to avoid conflict with the first subtask. This means the objective function associated with this subtask, g_2 , will be a function only of α , \mathbf{p}_A , and \mathbf{p}_G , ensuring orthogonality with the first subtask. The objective function can be defined as the square of the difference between the vehicle yaw angle α and a misalignment angle ζ :

$$g_2(\Psi) = (\alpha - \zeta)^2 \quad (43)$$

$$\zeta = \arctan\left(\frac{y_G - y_A}{x_G - x_A}\right) = \arctan\left(\frac{\delta_y}{\delta_x}\right) \quad (44)$$

$$\nabla g_2(\Psi) = 2(\alpha - \zeta) \begin{bmatrix} -\frac{\delta_y}{\delta_x^2 + \delta_y^2} & \frac{\delta_x}{\delta_x^2 + \delta_y^2} & 0 & 1 & \mathbf{0}_{1 \times 6} \end{bmatrix}^T \quad (45)$$

The third subtask is to maintain a desired manipulator pose during the travel and grasp preparation phase of executing the trajectory. The motivation for this subtask is to keep the arm in a pose that will be easy to hold during the faster travel phase, then switch to a high dexterity pose in preparation for completing a grasp. For a continuum manipulator, singularities occur only when θ_i equal zeros; the values of ϕ_i do not affect the total dexterity, so they can be neglected from the desired pose. The objective function g_3 can be defined as the squared norm of the manipulator pose error:

$$g_3(\Psi) = \|\Psi - \Psi_{\text{des}}\|^2 = (\Psi - \Psi_{\text{des}})^T (\Psi - \Psi_{\text{des}}) \quad (46)$$

$$\nabla g_3(\Psi) = \begin{bmatrix} \mathbf{0}_{2 \times 6} & 2 & \mathbf{0}_{2 \times 1} & 0 & \mathbf{0}_{2 \times 1} \end{bmatrix}^T (\Psi - \Psi_{\text{des}}) \quad (47)$$

$$\Psi = [\theta_1 \ \theta_2]^T \quad (48)$$

The definition of the desired pose Ψ_{des} is challenging because it changes as the end-effector approaches the target. To this end, a range threshold and desired pose for the travel phase, λ_{tra} and Ψ_{tra} , as well as a range threshold and desired pose for the preparation phase, λ_{pre} and Ψ_{pre} , are defined. In order to have a smooth transition between these poses, the fifth order smoothing polynomial $S(x, x_m, x_M)$ defined in Equation 37 is added:

$$\Psi_{\text{des}} = \Psi_{\text{pre}} + S\left(\frac{\delta_{\text{pre}} - \lambda_{\text{pre}}}{\lambda_{\text{tra}} - \lambda_{\text{pre}}}, \lambda_{\text{pre}}, \lambda_{\text{tra}}\right) (\Psi_{\text{tra}} - \Psi_{\text{pre}}) \quad (49)$$

$$\Psi_{\text{tra}} = [0 \ 0]^T \text{ rad}, \quad \Psi_{\text{pre}} = \left[-\frac{\pi}{4} \ \frac{\pi}{4}\right]^T \text{ rad} \quad (50)$$

Finally, the scaling parameters k_j are found empirically to achieve smooth and accurate performance in simulation. Objective function g_1 is to be maximized while g_2 and g_3 are to be minimized, so k_1 should be positive while k_2 and k_3 should be negative. In addition, k_3 should only apply throughout the travel and preparation phase of the trajectory, and be disabled during the final approach. This can be achieved by changing the value of the scaling parameter based on the position error:

$$k_1 = 3.0, \quad k_2 = -0.05, \quad k_3 = \begin{cases} -0.1 & \delta_p \geq \lambda_{\text{pre}} \\ 0 & \delta_p < \lambda_{\text{pre}} \end{cases} \quad (51)$$

It is worth noting that these subtask objective functions are, by inspection, orthogonal in the robot's configuration space, ensuring no conflict between subtasks. In cases where choosing orthogonal objective functions is not possible, a different optimization method such as the task priority method should be used, as discussed in Section 2.

5 Simulation Validation

To validate the algorithm proposed to resolve the redundancy of the free-floating vehicle system, two sets of kinematic simulations with multiple cases were performed using ROS Melodic Morenia and Python, with a time step of 0.01 seconds. The simulation was run on Ubuntu 18.04 with Intel Core i9-9900K @ 3.60 GHz and 16 GB DDR4 RAM. The first simulation analyzes the impact of the weighting matrix, and the second analyzes the impact of the gradient projection. The desired task for both simulations is simply to move the end-effector to a desired position of $\mathbf{p}_G = [1 \ 0 \ 0]^T$ m and orientation of $\mathbf{R}_G = \mathbf{R}_z(1 \text{ rad})$, imitating a basic grasp of an object at a known location. The z component of the goal orientation will require the robot to bend the end-effector in order to achieve this pose while still maintaining the field of

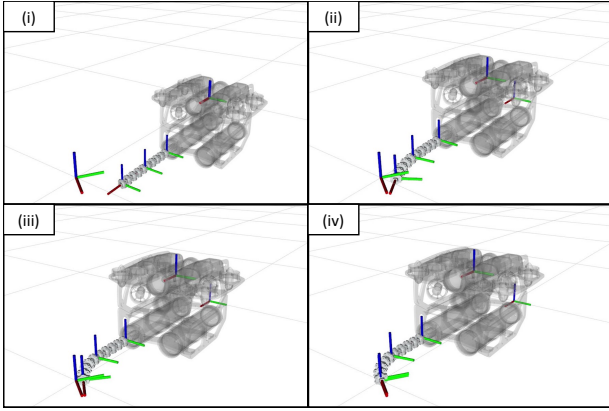


Fig. 5: Time-lapse of the optimized simulation trajectory.

view associated with the second subtask. A snapshot showing the continuum-UVMS, goal pose, and GCS is shown in Figure 4. A summary of the weighting matrix and gradient scaling parameters used for each case is contained in Table 1.

The weighting matrix comparison simulation was repeated for four cases in total. In Case 1, an identity matrix is used to equally weight all variables as a baseline for comparison. Case 2 shows the impact of manipulator prioritization using the constant weighting matrix \mathbf{W}_c defined in Equation 28. Case 3 introduces the joint limit weighting matrix \mathbf{W}_j as defined in Equation 32. Finally, Case 4 addresses dynamic manipulator prioritization by including the weighting matrix \mathbf{W}_m defined in Equation 35. All other simulation parameters are identical between cases, and all subtask objective functions are disabled by setting the scaling parameters k_j to zero.

The impact of each weighting matrix choice is demonstrated in Figures 6 and 7. As expected, the baseline case has the largest vehicle velocity commands while hardly utilizing the manipulator, as seen by the relatively low velocity commands. This is contrasted by much larger manipulator velocity and generally reduced vehicle velocities in Cases 2, 3, and 4. The introduction of the joint limit weighting matrix is best seen in the response of θ_2 in Cases 3 and 4, where the bending angle approaches but does not reach the minimum joint limit represented by a black horizontal line. The impact of the dynamic manipulator prioritization in Case 4 is subtle, but slightly higher linear vehicle velocities towards the beginning of the simulation and slightly higher manipulator bending velocities $\dot{\theta}_i$ towards the end can be seen. The impact of the weighting matrix choice is quantitatively compared in Table 2, which lists the average value of the vehicle velocities ($\bar{x}_A, \bar{y}_A, \bar{z}_A, \bar{\alpha}$) and manipulator bending velocities ($\bar{\theta}_1, \bar{\theta}_2$). Implementing the matrix \mathbf{W}_c shows a reduction in the average vehicle velocities between Cases 1 and 2 and increase in the magnitude of the manipulator bending velocity, particularly $\bar{\theta}_2$. Implementing \mathbf{W}_j shows a reduction in $\bar{\theta}_2$ between Cases 2 and 3 to avoid the joint limit on θ_2 . Finally, there is a small increase in magnitude of $\bar{\theta}_1$ and $\bar{\theta}_2$ between Cases 3 and 4 due to the introduction of \mathbf{W}_m to further prioritize the manipulator as the robot reaches the goal pose.

The impact of the GPM to optimize the proposed objective functions is the focus of the second simulation. To demonstrate this, the simulation was repeated for five cases. In Case 5, all of the objective functions were disabled by setting their respective scaling parameters k_j to zero in order to show the baseline solution without gradient projection. Next, Cases 6, 7, and 8 were run with only g_1 , only g_2 , and only g_3 enabled respectively to demonstrate the optimization of a single objective function at a time. In Case 9, all three objective functions were enabled to highlight the ability of the algorithm to handle multiple subtasks simultaneously. The total weighting matrix \mathbf{W} is included in each case. A time-lapse of the optimized trajectory solution to Equation 40 is shown in Figure 5.

The optimization of each cost function via the GPM is shown for each case in Figure 8. The baseline solution in Case 5 is, as expected, poorly optimized for all three subtasks, with small values of g_1 and large values of g_2 and g_3 . This trend is also evident in cases where the respective subtask is disabled; for example, Case 6 shows poor optimization of g_2 and g_3 . However, this case shows a significant improvement in optimization of g_1 . The impact of the gradient projection method is quantitatively compared in Table 3, which lists the average values of the cost functions under each case. Compared to the baseline Case 5, it can be clearly seen that Case 6 best maximizes g_1 , Case 7 best minimizes g_2 , and Case 8 best minimizes g_3 . In addition, combining all of the subtasks in Case 9 produces similar or better optimization of a given subtask than the corresponding single-subtask case.

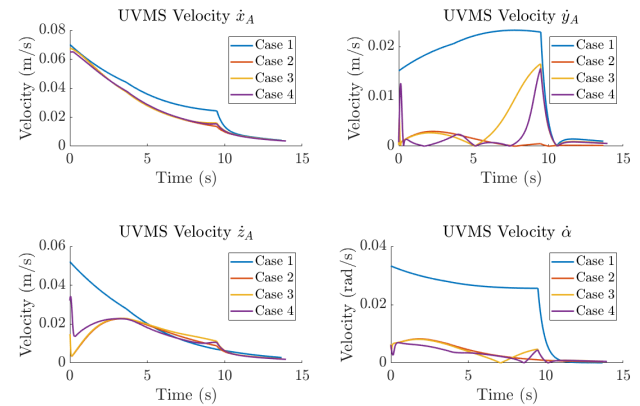


Fig. 6: Weighting matrix impact on UVMS velocity

6 Experimental Demonstration

6.1 Teleoperational Demonstration

The continuum-UVMS was deployed in the Davidson Laboratory towing tank at Stevens Institute of Technology. Initial testing of the UVMS was done using teleoperational control using a separate gamepad controller for each. This demonstrated three important capabilities. First, it showed

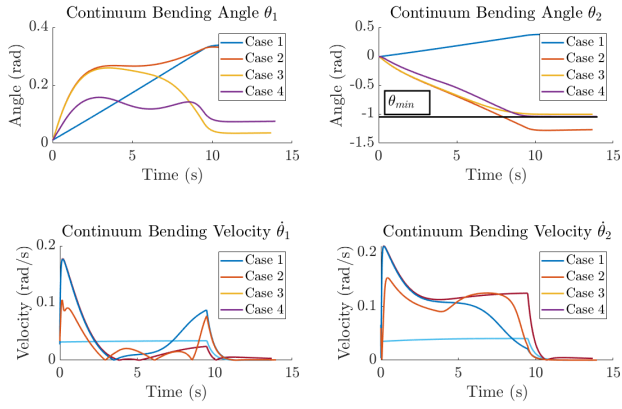


Fig. 7: Weighting matrix impacts on continuum position and velocity.

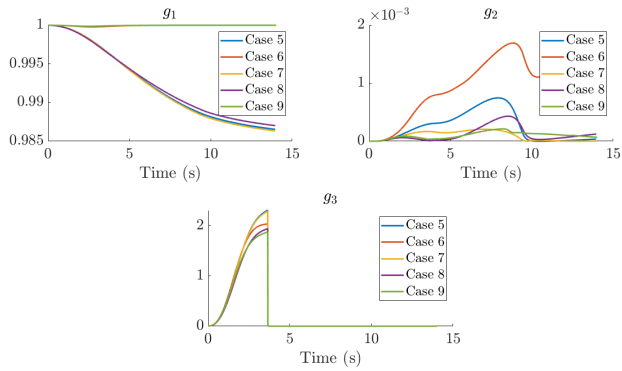


Fig. 8: Gradient projection impacts on optimizing objective functions.

Table 1: Simulation parameters for weighted least norm (WLN) and gradient projection method (GPM) on each case.

	Case	Weighting Matrix	k_1	k_2	k_3
WLN	1	\mathbf{I}	0	0	0
	2	\mathbf{W}_c	0	0	0
	3	$\mathbf{W}_c \mathbf{W}_j$	0	0	0
	4	$\mathbf{W}_c \mathbf{W}_j \mathbf{W}_m$	0	0	0
GPM	5	$\mathbf{W}_c \mathbf{W}_j \mathbf{W}_m$	0	0	0
	6	$\mathbf{W}_c \mathbf{W}_j \mathbf{W}_m$	3	0	0
	7	$\mathbf{W}_c \mathbf{W}_j \mathbf{W}_m$	0	-0.05	0
	8	$\mathbf{W}_c \mathbf{W}_j \mathbf{W}_m$	0	0	-0.1
	9	$\mathbf{W}_c \mathbf{W}_j \mathbf{W}_m$	3	-0.05	-0.1

the integrated continuum manipulator and vehicle were both waterproof. Second, it showed that communications between the manipulator, the vehicle, and the topside computer were successfully established. Third, it showed that arm movements had very little impact on the pose of the vehicle, which suggests that decoupling between the manipulator and the vehicle is a valid assumption. The experimental setup can be seen in Figure 9.

Table 2: Average value of vehicle and manipulator velocities for each case. Linear velocities \bar{x}_A , \bar{y}_A , and \bar{z}_A are in m/s, and angular velocities $\bar{\alpha}$, $\bar{\theta}_1$, and $\bar{\theta}_2$ are in rad/s.

Case	\bar{x}_A	\bar{y}_A	\bar{z}_A	$\bar{\alpha}$	$\bar{\theta}_1$	$\bar{\theta}_2$
1	0.0307	-0.0148	0.0182	0.0201	0.0240	0.0283
2	0.0256	0.0009	0.0122	0.0036	0.0224	-0.0917
3	0.0259	-0.0020	0.0128	0.0024	0.0019	-0.0724
4	0.0253	-0.0013	0.0127	0.0024	0.0047	-0.0738

Table 3: Average value of cost functions for each case.

Case	\bar{g}_1	\bar{g}_2	\bar{g}_3
5	0.9923	2.4711×10^{-4}	0.3053
6	1.0000	1.0017×10^{-3}	0.2928
7	0.9922	8.9955×10^{-5}	0.3039
8	0.9926	1.1569×10^{-4}	0.2674
9	1.0000	9.9368×10^{-5}	0.2661

6.2 Autonomous Trajectory Demonstration

A more sophisticated test of the continuum-UVMS is to autonomously execute the same trajectory simulated in Section 5, where the robot moves from rest to grasp a stationary target at a known location. The coordinated vehicle and manipulator commands are generated in real time on separate devices, kept in-sync via ROS. The vehicle commands are generated by the topside computer and include the linear velocity, which is executed using an open-loop velocity controller, and the goal orientation, which is executed using a closed-loop position controller with IMU feedback. The manipulator commands generated by the onboard computer are executed using a separate closed-loop position controller in the actuation unit microprocessor using built-in servomotor encoders. This experimental test provides a preliminary qualitative assessment of the feasibility of autonomous joint speeds distribution between the vehicle and the continuum manipulator. Due to the limitation of measurement equipment, validation of the trajectory accuracy is not considered.

A time lapse of the end-effector trajectory can be seen in Figure 10. The trajectory was captured using two underwater cameras, mounted perpendicularly to record both the global xz and global yz planes. The experimental trajectory of the arm is found by manually selecting the tip of the arm every 100 frames of the video playback. In Figure 10, the vehicle trajectory is shown in black, and the end-effector trajectory is shown in magenta. The experimental trajectory showed overshoot when compared with the simulated trajectory, but followed the general desired motion.

The vehicle commanded position is plotted against the experimental trajectory in Figure 11a. This plot indicates the vehicle drift which is not accounted for with the open-loop velocity control. In addition, overshoot in the Z direction of the vehicle is present which is likely due to the effects of buoyancy as the vehicle moves upwards during the trajectory. However, the positioning error of the manipulator relative to the base is more relevant to the scope of this paper and is shown in Figure 11b. This plot shows a much

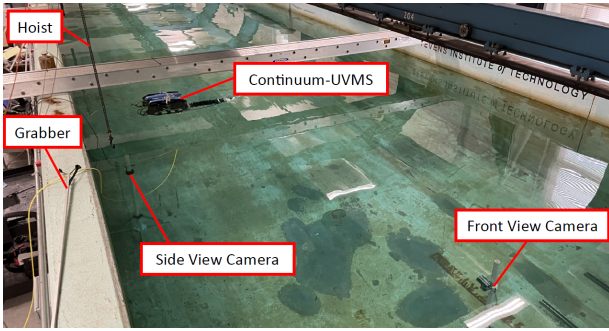


Fig. 9: Experimental setup in Davidson Laboratory towing tank.

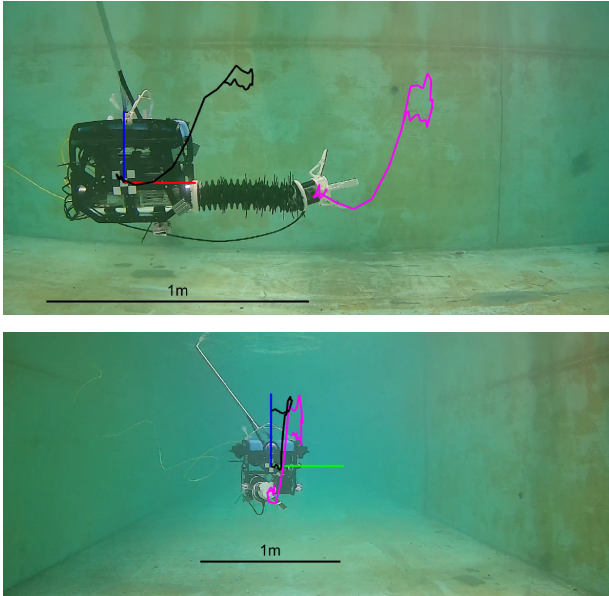
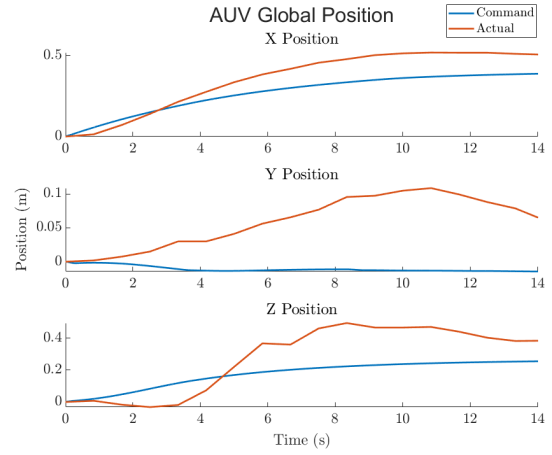


Fig. 10: Continuum-UVMS in experimental deployment, with vehicle and end-effector trajectory marked in black and magenta, respectively.

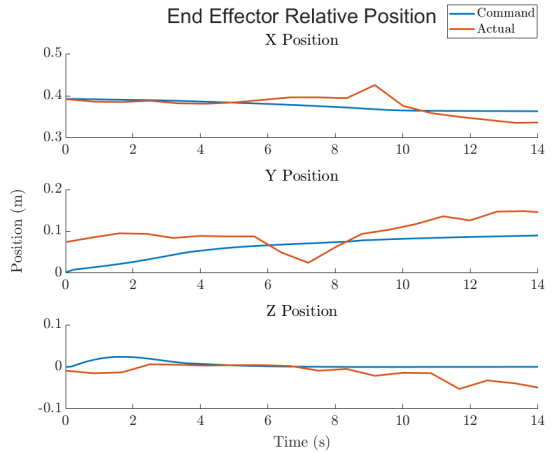
higher manipulator accuracy between the end-effector position command and the experimental trajectory. Error in each of the principal axes is kept within 0.05 m. This is comparable with the end-effector positioning error reported in Ambar et. al. [52], Cieslak et. al. [53], and Heshmati-Alamdari et. al. [54], whose reported error bounds are summarized in Table 4.

Table 4: End-effector experimental error comparison.

Publication	Error Bound
Ambar 2015	0.02 m
Cieslak 2015	0.02 m
Heshmati-Alamdari 2018	0.1 m
Our results	0.05 m



(a) Vehicle command vs. actual position.



(b) End-effector command vs. actual relative position.

Fig. 11: Experimental positioning error analysis.

6.3 Discussion

There are several limitations to these demonstrations, the most significant of which is the lack of a navigation system to accurately measure the vehicle's pose. The vehicle velocity commands were autonomously executed using only an open-loop controller, meaning that velocity error is not accounted for. While the experiments showed some degree of repeatability, accurate control is not possible. In addition, inertial and hydrodynamic effects are neglected in the controller, including the force and moment created by buoyancy and the constant backwards pull created by the tether. Testing also showed the vehicle's thruster speed controllers have a noticeable dead-band, which prevents small velocity commands from being actuated by the vehicle. Ultimately, a more robust and comprehensive low-level vehicle controller with a more advanced sensor suite for navigation could allow for precise and accurate trajectory generation, but the development of this low-level vehicle controller and navigation system is outside the scope of this paper.

7 Conclusion

This paper introduces the novel continuum-UVMS, a free-floating underwater vehicle with a continuum manipulator. The kinematics and total Jacobian matrix are mathematically derived as part of the kinematic control algorithm, which generates optimal trajectories. Choices of the objective functions for subtask optimization are discussed and compared in simulation. Mechanical, electrical, and software designs are introduced to explain the functionality of the entire system. The experimental deployment and demonstration of the continuum-UVMS are then presented, with sources of error in the vehicle control discussed as well.

Future work should include improvements to the vehicle closed-loop controller to increase vehicle velocity accuracy and consequently reduce end-effector positioning error, which is vital in many real-world applications. Better tuning of algorithm parameters may allow the robot to better balance speed and performance, as well as improve optimization of secondary objectives. Investigation of new and more sophisticated tasks, and choice of related secondary objectives to optimize such tasks, is an important research area to explore the capabilities of this system. Multi-manipulator planning may also be a lucrative research topic, with potential applications including dexterous underwater manipulation, perching, or climbing.

Acknowledgements

This research was supported in part by USDA-NIFA Grant No. 2021-67022-35977.

References

- [1] J. A. Trotter, C. Pattiaratchi, P. Montagna, M. Taviani, J. Falter, R. Thresher, A. Hosie, D. Haig, F. Fogliani, Q. Hua *et al.*, “First roV exploration of the perth canyon: Canyon setting, faunal observations, and anthropogenic impacts,” *Frontiers in Marine Science*, vol. 6, no. 173, 2019.
- [2] V. H. Fernandes, A. A. Neto, and D. D. Rodrigues, “Pipeline inspection with auv,” in *IEEE/OES Acoustics in Underwater Geosciences Symposium (RIO Acoustics)*, 2015, pp. 1–5.
- [3] P. Rundtop and K. Frank, “Experimental evaluation of hydroacoustic instruments for roV navigation along aquaculture net pens,” *Aquacultural Engineering*, vol. 74, pp. 143–156, 2016.
- [4] D. Ribas, P. Ridao, L. Magí, N. Palomeras, and M. Carreras, “The girona 500, a multipurpose autonomous underwater vehicle,” in *Oceans 2011 IEEE-Spain*. IEEE, 2011, pp. 1–5.
- [5] D. Ribas, N. Palomeras, P. Ridao, M. Carreras, and A. Mallios, “Girona 500 auv: From survey to intervention,” *IEEE/ASME Transactions on mechatronics*, vol. 17, no. 1, pp. 46–53, 2012.
- [6] J. Yuh, S. Choi, C. Ikehara, G. Kim, G. McMurty, M. Ghasemi-Nejhad, N. Sarkar, and K. Sugihara, “Design of a semi-autonomous underwater vehicle for intervention missions (sauvim),” in *Proceedings of 1998 international symposium on underwater technology*. IEEE, 1998, pp. 63–68.
- [7] G. Marani, S. K. Choi, and J. Yuh, “Underwater autonomous manipulation for intervention missions auvs,” *Ocean Engineering*, vol. 36, no. 1, pp. 15–23, 2009, autonomous Underwater Vehicles.
- [8] Blue Robotics, Inc., <https://bluerobotics.com/>, accessed: 2023-01-30.
- [9] W. J. Marais, S. B. Williams, and O. Pizarro, “Go with the flow: energy minimising periodic trajectories for uvms,” in *2022 International Conference on Robotics and Automation (ICRA)*. IEEE, 2022, pp. 01–07.
- [10] J. McConnell, F. Chen, and B. Englot, “Overhead image factors for underwater sonar-based slam,” *IEEE Robotics and Automation Letters*, vol. 7, no. 2, pp. 4901–4908, 2022.
- [11] D. Lane, J. Davies, G. Casalino, G. Bartolini, G. Cannata, G. Veruggio, M. Canals, C. Smith, D. O’Brien, M. Pickett, G. Robinson, D. Jones, E. Scott, A. Ferrara, D. Angelletti, M. Coccoli, R. Bono, P. Virgili, R. Pallas, and E. Gracia, “Amadeus: advanced manipulation for deep underwater sampling,” *IEEE Robotics & Automation Magazine*, vol. 4, no. 4, pp. 34–45, 1997.
- [12] M. Cianchetti, M. Calisti, L. Margheri, M. Kuba, and C. Laschi, “Bioinspired locomotion and grasping in water: The soft eight-arm octopus robot,” *Bioinspiration & Biomimetics*, vol. 10, 03 2015.
- [13] J. Liu, S. Iacoponi, C. Laschi, L. Wen, and M. Calisti, “Underwater Mobile Manipulation: A Soft Arm on a Benthic Legged Robot,” *IEEE Robotics & Automation Magazine*, vol. 27, no. 4, pp. 12–26, Dec 2020.
- [14] N. Ma, S. Monk, and D. Cheneler, “Design, prototyping and test of a dual-arm continuum robot for underwater environments,” in *2022 7th International Conference on Robotics and Automation Engineering (ICRAE)*. IEEE, 2022, pp. 158–164.
- [15] Z. Gong, B. Chen, J. Liu, X. Fang, Z. Liu, T. Wang, and L. Wen, “An opposite-bending-and-extension soft robotic manipulator for delicate grasping in shallow water,” *Frontiers in Robotics and AI*, vol. 6, 04 2019.
- [16] M. Hannan and I. Walker, “The ‘elephant trunk’ manipulator, design and implementation,” in *2001 IEEE/ASME International Conference on Advanced Intelligent Mechatronics. Proceedings (Cat. No. 01TH8556)*, vol. 1. IEEE, 2001, pp. 14–19.
- [17] M. W. Hannan and I. D. Walker, “Kinematics and the implementation of an elephant’s trunk manipulator and other continuum style robots,” *Journal of robotic systems*, vol. 20, no. 2, pp. 45–63, 2003.
- [18] P. Ridao, M. Carreras, D. Ribas, P. J. Sanz, and G. Oliver, “Intervention auvs: the next challenge,” *Annual Reviews in Control*, vol. 40, pp. 227–241, 2015.
- [19] N. Palomeras, A. Penalver, M. Massot-Campos, G. Vallicrosa, P. L. Negre, J. J. Fernández, P. Ridao, P. J. Sanz, G. Oliver-Codina, and A. Palomer, “I-auv docking and intervention in a subsea panel,” in *2014 IEEE/RSJ international conference on intelligent robots and sys-*

- tems. IEEE, 2014, pp. 2279–2285.
- [20] D. Ribas, P. Ridao, A. Turetta, C. Melchiorri, G. Palli, J. J. Fernández, and P. J. Sanz, “I-avv mechatronics integration for the trident fp7 project,” *IEEE/ASME Transactions on Mechatronics*, vol. 20, no. 5, pp. 2583–2592, 2015.
- [21] N. Sarkar and T. K. Podder, “Coordinated motion planning and control of autonomous underwater vehicle-manipulator systems subject to drag optimization,” *IEEE Journal of Oceanic Engineering*, vol. 26, no. 2, pp. 228–239, 2001.
- [22] F. Yu, Q. Zhu, and Y. Chen, “Adaptive fractional-order fast-terminal-type sliding mode control for underwater vehicle-manipulator systems,” *Journal of Mechanisms and Robotics*, vol. 15, no. 6, p. 064501, 2023.
- [23] A. Liegeois *et al.*, “Automatic supervisory control of the configuration and behavior of multibody mechanisms,” *IEEE transactions on systems, man, and cybernetics*, vol. 7, no. 12, pp. 868–871, 1977.
- [24] I. D. Walker and S. I. Marcus, “Subtask performance by redundancy resolution for redundant robot manipulators,” *IEEE Journal on Robotics and Automation*, vol. 4, no. 3, pp. 350–354, 1988.
- [25] Y. Liu, J. Zhao, and B. Xie, “Obstacle avoidance for redundant manipulators based on a novel gradient projection method with a functional scalar,” in *2010 IEEE International Conference on Robotics and Biomimetics*. IEEE, 2010, pp. 1704–1709.
- [26] S. B. Slotine and B. Siciliano, “A general framework for managing multiple tasks in highly redundant robotic systems,” in *proceeding of 5th International Conference on Advanced Robotics*, vol. 2, 1991, pp. 1211–1216.
- [27] S. Moe, G. Antonelli, A. R. Teel, K. Y. Pettersen, and J. Schrimpf, “Set-based tasks within the singularity-robust multiple task-priority inverse kinematics framework: General formulation, stability analysis, and experimental results,” *Frontiers in Robotics and AI*, vol. 3, p. 16, 2016.
- [28] T. F. Chan and R. V. Dubey, “A weighted least-norm solution based scheme for avoiding joint limits for redundant joint manipulators,” *IEEE Transactions on Robotics and Automation*, vol. 11, no. 2, pp. 286–292, 1995.
- [29] S. Soylu, B. J. Buckham, and R. P. Podhorodeski, “Redundancy resolution for underwater mobile manipulators,” *Ocean Engineering*, vol. 37, no. 2-3, pp. 325–343, 2010.
- [30] F. Flacco, A. De Luca, and O. Khatib, “Motion control of redundant robots under joint constraints: Saturation in the null space,” in *IEEE International Conference on Robotics and Automation*, 2012, pp. 285–292.
- [31] H. Xing, Z. Gong, L. Ding, A. Torabi, J. Chen, H. Gao, and M. Tavakoli, “An adaptive multi-objective motion distribution framework for wheeled mobile manipulators via null-space exploration,” *Mechatronics*, vol. 90, no. 102949, 2023.
- [32] T. K. Podder and N. Sarkar, “A unified dynamics-based motion planning algorithm for autonomous underwater vehicle-manipulator systems (uvms),” *Robotica*, vol. 22, no. 1, pp. 117–128, 2004.
- [33] S. Soylu, B. J. Buckham, and R. P. Podhorodeski, “Dexterous task-priority based redundancy resolution for underwater manipulator systems,” *Transactions of the Canadian Society for Mechanical Engineering*, vol. 31, no. 4, pp. 519–533, 2007.
- [34] G. Casalino, E. Zereik, E. Simetti, S. Torelli, A. Sperindé, and A. Turetta, “Agility for underwater floating manipulation: Task & subsystem priority based control strategy,” in *2012 IEEE/RSJ International Conference on Intelligent Robots and Systems*. IEEE, 2012, pp. 1772–1779.
- [35] G. Antonelli, *Underwater Robots - motion and force control of vehicle-manipulator systems*, 2nd ed. Germany: Springer International Publishing, 2006.
- [36] E. Simetti, G. Casalino, S. Torelli, A. Sperinde, and A. Turetta, “Floating underwater manipulation: Developed control methodology and experimental validation within the trident project,” *Journal of Field Robotics*, vol. 31, no. 3, pp. 364–385, 2014.
- [37] J. J. Fernández, M. Prats, P. J. Sanz, J. C. García, R. Marin, M. Robinson, D. Ribas, and P. Ridao, “Grasping for the seabed: Developing a new underwater robot arm for shallow-water intervention,” *IEEE Robotics & Automation Magazine*, vol. 20, no. 4, pp. 121–130, 2013.
- [38] Y. Wang, S. Wang, Q. Wei, M. Tan, C. Zhou, and J. Yu, “Development of an underwater manipulator and its free-floating autonomous operation,” *IEEE/ASME Transactions on Mechatronics*, vol. 21, no. 2, pp. 815–824, 2015.
- [39] Reach Robotics, <https://reachrobotics.com/>, accessed: 2023-07-05.
- [40] Y. Fang, X. Dong, A. Mohammad, and D. Axinte, “Design and control of a multiple-section continuum robot with a hybrid sensing system,” *IEEE/ASME Transactions on Mechatronics*, vol. 28, no. 3, pp. 1522–1533, 2023.
- [41] W. S. Rone, W. Saab, and P. Ben-Tzvi, “Design, Modeling, and Integration of a Flexible Universal Spatial Robotic Tail,” *Journal of Mechanisms and Robotics*, vol. 10, no. 4, 2018.
- [42] Y.-m. Na, H.-s. Lee, and J.-k. Park, “Fabrication and Experiment of an Automatic Continuum Robot System Using Image Recognition,” *Journal of Mechanisms and Robotics*, vol. 12, no. 1, pp. 1–9, Feb 2020.
- [43] Y. Liu, Z. Ge, S. Yang, I. D. Walker, and Z. Ju, “Elephant’s Trunk Robot: An Extremely Versatile Under-Actuated Continuum Robot Driven by a Single Motor,” *Journal of Mechanisms and Robotics*, vol. 11, no. 5, 2019.
- [44] W. McMahan, V. Chitrakaran, M. Csencsits, D. Dawson, I. D. Walker, B. A. Jones, M. Pritts, D. Dienno, M. Grissom, and C. D. Rahn, “Field trials and testing of the octarm continuum manipulator,” in *Proceedings 2006 IEEE International Conference on Robotics and*

- Automation, 2006. ICRA 2006.* IEEE, 2006, pp. 2336–2341.
- [45] J. B. C. Davies, D. Lane, G. Robinson, D. O’Brien, M. Pickett, M. Sfakiotakis, and B. Deacon, “Subsea applications of continuum robots,” in *Proceedings of 1998 International Symposium on Underwater Technology*. IEEE, 1998, pp. 363–369.
- [46] T. Zheng, D. T. Branson, E. Guglielmino, R. Kang, G. A. Medrano Cerda, M. Cianchetti, M. Follador, I. S. Godage, and D. G. Caldwell, “Model Validation of an Octopus Inspired Continuum Robotic Arm for Use in Underwater Environments,” *Journal of Mechanisms and Robotics*, vol. 5, no. 2, pp. 1–11, 2013.
- [47] J. L. Sittler and L. Wang, “A Modular Open-Source Continuum Manipulator for Underwater Remotely Operated Vehicles,” *Journal of Mechanisms and Robotics*, vol. 14, no. 6, 04 2022.
- [48] L. Wang, “Open source modular continuum robot project,” <https://longwang.in/modular-continuum-manipulator/>, 2022, accessed: 2023-01-30.
- [49] Y. Tlegenov, K. Telegenov, and A. Shintemirov, “An open-source 3d printed underactuated robotic gripper,” in *2014 IEEE/ASME 10th International Conference on Mechatronic and Embedded Systems and Applications (MESA)*. IEEE, 2014, pp. 1–6.
- [50] Open Robotics, “ROS - Robot Operating System,” <https://www.ros.org>, accessed: 2023-01-30.
- [51] J. McConnell, “BlueROV2 Heavy ROS Package,” <https://github.com/jake3991/Argonaut>, accessed: 2023-01-30.
- [52] R. B. Ambar, S. Sagara, and K. Imai, “Experiment on a dual-arm underwater robot using resolved acceleration control method,” *Artificial Life and Robotics*, vol. 20, pp. 34–41, 2015.
- [53] P. Cieslak, P. Ridao, and M. Giergiel, “Autonomous underwater panel operation by girona500 uvms: A practical approach to autonomous underwater manipulation,” in *2015 IEEE International conference on robotics and automation (ICRA)*. IEEE, 2015, pp. 529–536.
- [54] S. Heshmati-Alamdari, C. P. Bechlioulis, G. C. Karras, A. Nikou, D. V. Dimarogonas, and K. J. Kyriakopoulos, “A robust interaction control approach for underwater vehicle manipulator systems,” *Annual Reviews in Control*, vol. 46, pp. 315–325, 2018.